Cement and Concrete Composites 88 (2018) 52–63

Contents lists available at ScienceDirect

Cement and Concrete Composites

journal homepage: www.elsevier.com/locate/cemconcomp

Use of tomography to understand the influence of preconditioning on carbonation tests in cement-based materials

Dong Cui [a, b, *], Wei Sun [a], Nemkumar Banthia [b]

[a] School of Material Science and Engineering, Southeast University, Nanjing 211189, People's Republic of China
[b] School of Civil Engineering, University of British Columbia, Vancouver V6T 1Z4, Canada

ARTICLE INFO

Article history:
Received 1 September 2017
Received in revised form
13 January 2018
Accepted 26 January 2018
Available online 31 January 2018

Keywords:
Cement-based materials
Carbonation
Computer tomography(CT)
Preconditioning
Durability
Global climate change

ABSTRACT

Recognition of the rising amount of atmospheric CO_2 has brought renewed interest in understanding the effects of carbonation on reinforced concrete performance. In laboratory testing, the specimens must be preconditioned to effectively study carbonation. This paper studied the influence of several preconditioning schemes on the carbonation profiles of cement paste specimens subjected to accelerated carbonation tests. The evolution of microstructure and moisture during carbonation were investigated accordingly. Bulk of the work was based on an extended X-ray attenuation method (XRAM), which relied on X-ray computed tomography (CT). A novel method was introduced to evaluate the extent of damage due to drying. Based on extent of damage, the paper recommends standard-cured specimens for carbonation tests as compared to water-cured specimens. Also, when comparing between oven drying and mass balancing, the latter was shown to be more suitable, as the inner moisture distribution becomes more uniform after this drying protocol, and less fluctuation of humidity will occur during carbonation.

© 2018 Elsevier Ltd. All rights reserved.

1. Introduction

Concrete carbonation occurs when atmospheric CO_2 and pore water react with calcium-bearing products of cement hydration. The process leads to reduced pH of the hydrated pastes, which will further accelerate the corrosion of imbedded reinforcement. To design infrastructure with adequate durability, a number of investigations have been carried out to understand the mechanisms of carbonation and to predict its speed [1–8]. With increased CO_2 concentration in atmosphere associated with global warming, the current carbonation speeds are faster than ever. Accordingly, there is a renewed interest in understanding the effects and speed of carbonation [1–4]. Infrastructures are designed to be in service for decades, and it is therefore impractical to conduct an on-site carbonation test that at natural speeds will last for a very long period of time. To be efficient, in laboratory, accelerated carbonation tests are routinely performed where specimens are carbonated in a carbonation chamber with elevated temperatures, high CO_2 concentrations and critical values of relative humidity (RH) [5–7].

Test specimens are often in a saturated state after curing, and carbonation tests are therefore, difficult to be performed due to limited available pore volume for CO_2 diffusion. For that reason, preconditioning must be performed to lower inner RH to an intermediate level (40–70%) [4,8]. In most circumstances, intermediate RH is achieved through drying under an elevated temperature [9–13]. Although previous work has proven the effectiveness of oven drying, there is already some concern on the application of oven drying, as the method has the potential to damage the specimen [14,15]. In addition, oven drying may excessively dry the surface, while leaving a considerable amount of water near the core of the specimen, under which circumstance the inner moisture distribution may not be uniform [16–18].

Realizing these drawbacks, some researchers have tried to achieve an intermediate RH by conditioning the specimen in an environmental chamber [13,19,20]. Compared with oven drying, this protocol appears to be more amicable. Based on the authors' knowledge, only a few attempts have been made so far to validate the effectiveness of such protocol, and the extent of damage caused, if any, is not fully known.

In order to trace the moisture evolution, previous researchers have done some pioneering work. For instance, Turcry et al. [18] investigated the inner RH through RH probes buried during casting,

* Corresponding author. School of Material Science and Engineering, Southeast University, Nanjing 211189, People's Republic of China.
E-mail address: 230119337@seu.edu.cn (D. Cui).

https://doi.org/10.1016/j.cemconcomp.2018.01.011
0958-9465/© 2018 Elsevier Ltd. All rights reserved.

and the evolution of inner RH was revealed from the probes. The work itself offered new insights into the moisture behavior, but the results may be different without probes, as RH probes blocked the path for moisture and gas migration, and the transmission behavior might be different without the probes. Also, strictly speaking, RH probes are only capable of measuring the RH between the probe and the specimen. In recent years, the attenuation method has been used for carbonation investigations, and some interesting work was carried out by Morandeau et al. [16,17]. Based on their work, the inner RH was far from equilibrium after traditional preconditioning schemes, and more suitable preconditioning schemes are therefore, required.

The traditional attenuation method is highly versatile. Chemical changes, microstructure evolution and moisture evolution can all be characterized. Besides, compared with traditional testing techniques like scanning electron microscopy (SEM) [21–23] or mercury intrusion porosimetry (MIP) [24–26], sample preparation is unnecessary in attenuation method, so the characterized microstructure (damage) should be closer to that of intact specimen. Moreover, since local moisture content can be quantified by attenuation method without sectioning, the measured moisture content should be more reliable compared with that based on traditional methods [27,28]. Despite the benefits, traditional attenuation method has limitations [29]: traditional attenuation method only offers the attenuation coefficient of the whole scanned area, while for a local zone within the area, its attenuation coefficient is unmeasurable. In this paper, X-ray computed tomography (XCT) was combined with the attenuation method, which extended the traditional attenuation method to three-dimensions. The level of precision was therefore, improved, and both a spatial distribution of carbonation product and evolution of microstructure could be characterized. The extended X-ray attenuation method (XRAM) has been used by Wan et al. for the investigation of carbonation product [29] and microstructure of a partly leached paste [30]. Further, in this paper, a combination of mercury intrusion porosimetry (MIP), thermo-gravimetric analysis (TGA), extended XRAM, was adopted to understand the chemical changes and microstructure and moisture evolution occurring in specimen during carbonation as a function of preconditioning. To the authors' knowledge, this is the first use of extended attenuation method for the evaluation of carbonation preconditioning schemes. The work aims at determining the most suitable preconditioning protocol, which offers a uniform moisture distribution and introduces minimal damage. In addition, an optimal preconditioning scheme guarantees minimal fluctuation of RH during carbonation, and the process can thus be regarded being performed under a constant humidity level.

2. Experimental protocol

2.1. Specimen preparation and curing

The cement used in this study was one P·II cement manufactured from Huaxin cement factory. The chemical composition of cement is listed in Table 1.

The water to cement ratio in this study was 0.5, and all specimens were (i) cast in moulds of $40 \times 40 \times 160\,mm^3$; (ii) covered with plastic sheets for 24 h at ambient conditions; (iii) de-moulded and cured for 28 days. Two curing conditions were selected in this study:

Standard-Cured: Half of the specimens were cured in a standard curing room ($20 \pm 1\ ^\circ C$, and RH of above 95%).

Water-Cured: The other half were cured at $20 \pm 1\ ^\circ C$ in lime-saturated solution.

Table 1
Chemical composition of cement/wt%.

CaO	SiO_2	Al_2O_3	Fe_2O_3	P_2O_5	SO_3	Others	LOI	Total
52.18	23.49	8.12	3.38	6.41	5.22	0.70	0.50	100.00

2.2. Conditioning

When the curing procedure was complete, all specimens were taken immediately for drying. Two drying protocols were adopted in this study: specimens were either dried in a vacuum oven (under $60\ ^\circ C$) for 48 h, or dried in an environmental chamber (under $20 \pm 1\ ^\circ C$, 65% RH, and nitrogen was injected periodically to avoid air carbonation) for 6 months. To accelerate the RH equilibrium process, some of the specimens were cut into slices with a thickness of 9 mm. The schematic for specimens is shown in Fig. 1, and the mass evolution of the specimens under both drying conditions is illustrated in Fig. 2.

After the drying procedure, epoxy resin was used to cover five faces of each specimen, leaving one for carbonation (see Fig. 1). In particular, for each sliced specimen, the casting face ($40 \times 9\,mm^2$), the bottom face ($40 \times 9\,mm^2$) and three lateral faces (two $40 \times 40\,mm^2$ and one $40 \times 9\,mm^2$) were sealed, leaving one ($40 \times 9\,mm^2$) open to carbonation. For each rectangular specimen, the casting face ($40 \times 160\,mm^2$), the bottom face ($40 \times 160\,mm^2$), and three lateral faces (two $40 \times 40\,mm^2$ and one $40 \times 160\,mm^2$) were sealed, leaving one ($40 \times 160\,mm^2$) for carbonation. In the following, the standard-cured and mass-balanced specimen were denoted as “SR”; the water-cured and mass-balanced specimens were denoted as “WR”; the standard-cured and oven-dried specimens were denoted as “SO”; and the water-cured and oven-dried specimens were denoted as “WO”.

2.3. Accelerated carbonation test

The carbonation test was performed according to China standard GB T50082-2009 [31]. The climate inside the carbonation chamber was: $20 \pm 2\ ^\circ C$, $70 \pm 5\%$ RH and $20 \pm 3\%$ CO_2 concentration. The specimens at 2 days, 7 days, 14 days and 28 days of carbonation were taken successively for analysis.

2.4. Experimental methodology

2.4.1. Phenolphthalein spray test

Phenolphthalein spray test has been adopted worldwide for the measurement of carbonation depth [3,9–11], and the test is performed by spraying the freshly split faces with the phenolphthalein indicator. The indicator will remain pink fuchsia when the pH is higher than 10, while turning colorless when the pH falls below 8.3.

2.4.2. Mercury intrusion porosimetry (MIP)

Mercury Intrusion Porosimetry (MIP) test was performed with one Autopore 9500 in this study. The contact angle was assumed to be 130°. The pressure applied in this study ranged from 0.003 MPa to 242 MPa, which related to pore radii ranging from 180 μm down to 3 nm.

2.4.3. X-ray attenuation method (XRAM)

X-ray attenuation method (XRAM) was adopted in this study for the investigation of chemical composition, moisture migration and porosity evolution. The methodology for XRAM has been depicted extensively elsewhere [29,30,32,33]. Here, a brief introduction is given.

In XRAM, the calcium carbonate ($C\overline{C}$) content is measured

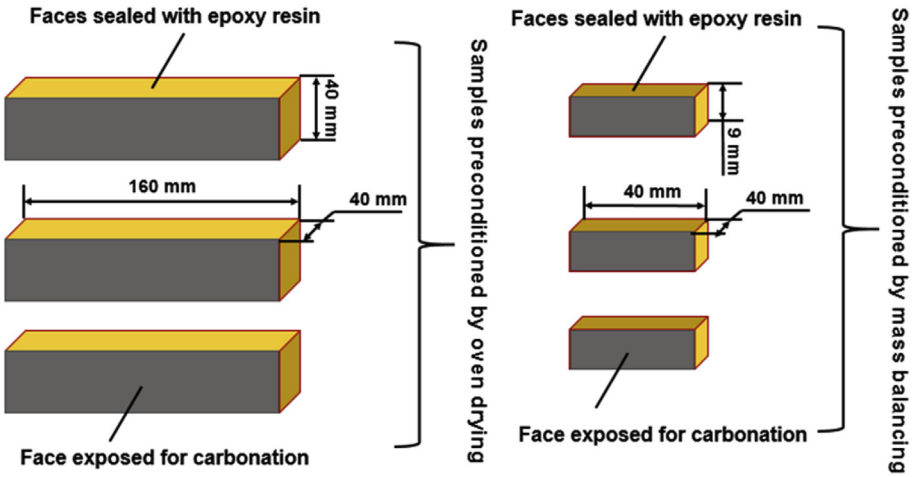

Fig. 1. Schematic of specimens prepared for accelerated carbonation tests.

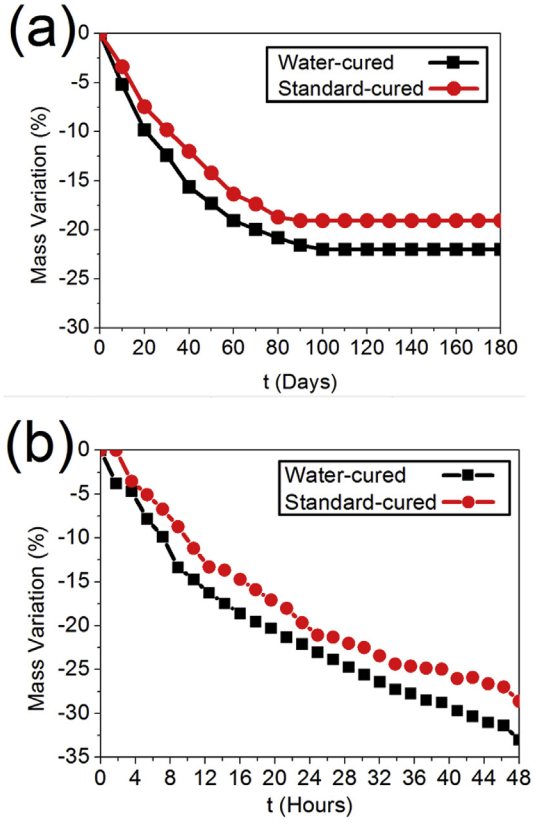

Fig. 2. Mass variation vs. drying time. (a) Specimens dried in an environmental chamber; (b) Specimens dried in an oven. The RH equilibrium was achieved at approximately 100 days for (a); however, no RH equilibrium was achieved during the drying period for (b).

through multiple scans on the specimen at variant carbonation ages. The parameters of all CT scans were kept constant, in which case the local $C\overline{C}$ content can be deduced through Eq. (1) [29].

$$f_{CaCO_3}(x,y,z) = \frac{G_{after}(x,y,z) - G_{before}(x,y,z)}{G_{CaCO_3} - (1 - \frac{38}{369})G_{Ca(OH)_2}} \quad (1)$$

where, $G_{before}(x,y,z)$ and $G_{after}(x,y,z)$ are the gray-scale values of the voxel before and after carbonation, respectively; G_{CaCO_3} and $G_{Ca(OH)_2}$ represent the gray-scale values of $C\overline{C}$ and calcium hydroxide (CH), respectively.

For local porosity, it was deduced through dual scan of the specimen in the saturated state and in the dried state, respectively, as expressed by Eq. (2) [30,32–34].

$$w_{pore} = \frac{G_{sat} - G_{dry}}{G_{water} - G_{air}} \quad (2)$$

where, w_{pore} is the local porosity. G_{sat} and G_{dry} are the gray-scale values of the specimen in the saturated state and in the dried state, respectively. G_{water} and G_{air} are the gray-scale values of water and air, respectively.

Inheriting the methodology applied for porosity calculation, and substituting the saturated state with the original state; in other words, apply an additional CT scan right after preconditioning or right after carbonation, the local water content can also be deduced, as expressed by Eq. (3).

$$W = \frac{G_{ori} - G_{dry}}{G_{water} - G_{air}} \quad (3)$$

where, W is the volume fraction of water from one voxel, and G_{ori} is the gray-scale value of the specimen in the original state and in the dried state.

It should be noted here that it is inevitable to have some displacement during multiple scans, therefore, a registration strategy developed by Latham et al. [35] was applied here for data alignment of CT data from variant scans. According to Eqs. (1)–(3), to obtain chemical composition, porosity and moisture content, each specimen should be scanned for three times: the first scan is performed immediately after curing or at variant carbonation age; the second scan is performed in the saturated state; and the last scan is performed in the dried state. The saturated state was achieved by immersing the specimen in boiled and cooled water for two weeks, and a pump with a working force of 1.5 CFM was used to drive the air out from the specimen. To accelerate the saturation process, all specimens were sectioned into slices with a thickness of ~5 mm. The dried state was achieved through conditioning the specimen in a vacuum oven under 45 °C for two weeks.

The CT device used in this study was manufactured from Yxlon in Germany. For all scans, the X-ray peak energy was 195 kV, the current was 0.3 mA. The acquisition time was 8 s per projection, and the effective resolution was 60 μm.

3. Results

3.1. Carbonation depth measured through phenolphthalein spray test

Fig. 3 presents the carbonation depth as a function of square of carbonation age. It is evident that, oven-dried specimens carbonated faster at early carbonation age (before 7 days). To be specific, the carbonation depth was approximately 8 mm and 10 mm respectively for WO and SO after 2 days of carbonation, while at the same age, the carbonation depth of WR and SR was merely 6 mm and 3 mm. SO specimen maintained a high carbonation speed throughout the test, while in the case of WO specimen, the WR specimen caught up in terms of the carbonation depth at 7 days, and eventually, the carbonation depth was surpassed by WR specimen at 14 days.

Fig. 3 also reveals two opposite carbonation trends based on different drying protocols: after oven drying, standard-cured specimens carbonated faster; while after mass balancing, water-cured specimens carbonated faster. The opposite trends suggest that, both curing strategy and the drying protocol have a significant effect on the carbonation speed, and the measured carbonation depth was resulted from the coupled effect of both factors.

It should be noted that the measurement of carbonation depth was stopped at 14 days for mass-balanced specimens, which is due to the fact that in its case, the carbonation depth was detected to be significantly exaggerated due to side carbonation at that age. Side carbonation is described as the carbonation that progressed from the faces sealed with epoxy resin. Even though epoxy resin was carefully smeared on all lateral faces to prevent side carbonation, the process cannot be fully prevented, as the cracks on lateral faces went deeper beneath the surface. Side carbonation can be ignored for bulk specimens (e.g. oven-dried specimens), as the carbonation depth in their case is usually of the order of millimeters (see Figs. 4 and 6), which can be ignored compared with the specimen size. For mass-balanced specimens, on the other hand, since the specimens themselves are of the order of millimeters, ignoring side carbonation will result in exaggerated carbonation depths, especially after 14 days.

3.2. 2D and 1D $\overline{CC}$ distribution obtained through XRAM

Fig. 4 presents the 2D distributions of $\overline{CC}$ for SO and WO specimens, respectively. Compared with WO, the carbonation rate of SO was higher. This result is in accordance with the result from phenolphthalein spray test (see Fig. 3), and similar results have been reported previously, where finer microstructure of water-cured specimen was addressed as the main cause of the slower carbonation rate [36].

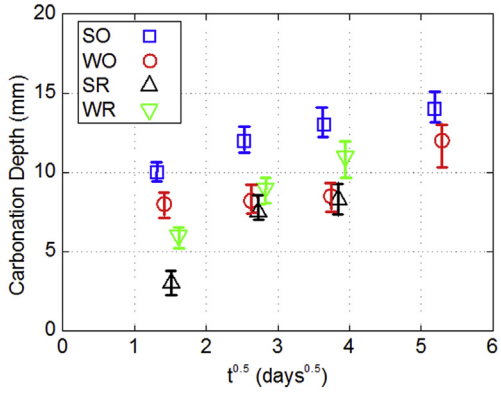

Fig. 3. Carbonation depth as a function of the carbonation age measured through phenolphthalein spray test.

As shown in Fig. 4(d), the surface of the carbonation face appears darker than the inside. The most plausible reason for this is excessive dryness. The main goal of oven drying is to partially remove the water from the pores, as CO_2 would preferentially transport through gaseous paths; however, to support carbonation, water is still required, as CO_2 binding only takes place in the aqueous environment. After thermal pretreatment, the specimen surface was excessively dried, even though gaseous CO_2 was bound to pass through sample surface for carbonation, the gas could not be bound by the matrix due to lack of water. The non-carbonated surface was no longer observable at 7 days (see Fig. 4(e)), which confirms that excessive dryness was limited to early carbonation ages, and the water near specimen surface was recovered in a few days.

The excessive dryness due to oven drying has been reported previously [18]; and, the phenomenon can lead to overestimation on early-age carbonation depths: as the specimen surface was drier, the gaseous space in pores increased, and CO_2 transmission under that circumstance would be easier. The CO_2 could transmit to deeper area and be bound at the place where RH was suitable for carbonation, leading to larger carbonation depths.

Fig. 4 only offers a qualitative result of the $\overline{CC}$ distribution. To be quantitative, 1D $\overline{CC}$ profile is required. The 1D profiles are shown in Fig. 5. For an instant $\overline{CC}$ profile, it was read along the line profile of its related 2D rendering (a typical line that was used for $\overline{CC}$ calculation is illustrated as AA′ in Fig. 4). Considering that the resolution of all scans was 60 μm, each point from an instant profile only represented a cubic area with side of 60 μm, which was non-representative. To mitigate the fluctuation of the profiles, for each profile presented in Fig. 5, it is the average result of 5000 instant profiles.

As shown in Fig. 5, an advancing front-end is revealed on the $\overline{CC}$ profiles with increased carbonation age, which supports the continuation of carbonation. Besides, the $\overline{CC}$ content is lower near the surface at 2 days of carbonation, which points out once again the existence of excessive dryness as discussed before.

At 2 days of carbonation, the carbonation depth for both SO and WO attained approximately 10 mm, which occupied nearly half of the carbonation depth at 28 days of carbonation. The result is in line with the carbonation depths in Figs. 3 and 4, and the result attests that oven drying is not an ideal protocol if early-age carbonation behavior is to be studied.

To further attest the reliability of XRAM, $\overline{CC}$ content was measured by TGA, and the results are shown as purple bars in Fig. 5. The $\overline{CC}$ content measured from TGA is at a similar order of magnitude with that from XRAM, which validates the reliability of XRAM in chemical analysis. Nonetheless, the deficiency of XRAM is also clear, as strictly speaking, the $\overline{CC}$ content obtained from XRAM was slightly higher than that obtained from TGA, especially in WO specimens. The overestimation did not result from the methodology of XRAM, but from the assumption we made in chemical analysis: in our assumption, all variation of attenuation coefficient during multiple scans was accounted as "CO_2 binding", and no moisture migration was taken into consideration. Such an assumption was tenable for systems involving mild moisture movement; however, for systems containing drastic moisture migration (for instance, significant supplement of moisture in WO), the increased attenuation coefficient by moisture absorption, would be mistakenly accounted as "CO_2 binding", leading to an overestimated $\overline{CC}$ content.

In a strict sense, two other factors may also decrease the reliability of chemical results based on XRAM: first, simplified

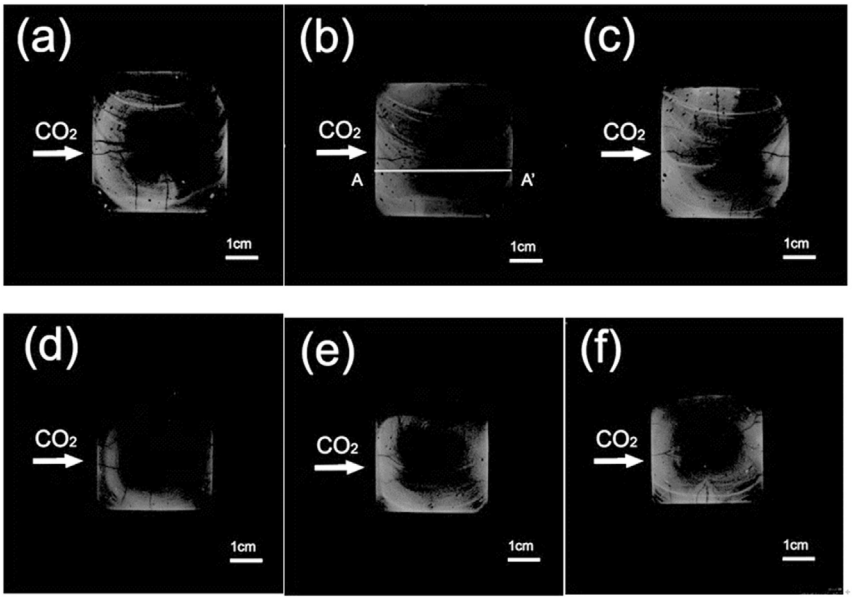

Fig. 4. 2D $C\overline{C}$ renderings at variant carbonation ages. (a), (b), (c) refer to SO after 2 days, 7 days and 14 days of carbonation, respectively, and (d), (e), (f) refer to WO after 2 days, 7 days and 14 days of carbonation, respectively.

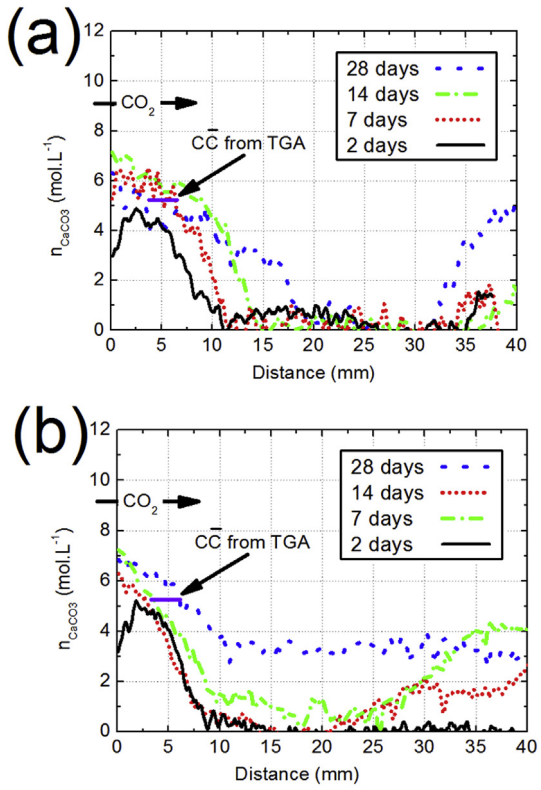

Fig. 5. 1D $C\overline{C}$ profiles for (a) SO and (b) WO. The purple bar represents the $C\overline{C}$ content measured through TGA at 28 days. (For interpretation of the references to color in this figure legend, the reader is referred to the Web version of this article.)

carbonation product was considered in this study. In most circumstances while calcite, vaterite, aragonite and amorphous $C\overline{C}$ coexist after carbonation [37,38]; in this study, only calcite was taken into consideration. The simplification would introduce approximately 10% error in the calculated $C\overline{C}$, but the error level was likely much smaller compared to the total $C\overline{C}$ generated by carbonation [17]. Also, please note that an accelerated carbonation condition was adopted in this work, where calcite is proven to be the predominant carbonation product [39]; and, second, beam hardening artifact [40] will disturb the results. Since the X-rays used for CT scan is a flux of variant wavelengths, some soft part (with lower energy) may be absorbed by the scanned object during transmission. However, in the reconstruction system, X-rays are assumed as a flux of constant wavelength, and no absorption was taken into consideration. The assumption leads to overestimation of the attenuation coefficient near the specimen surface, so the surface of the scanned object always appears to be brighter in reconstructed CT images. Beam hardening artifact affects the local attenuation coefficient, which will further lower the accuracy of quantitative analysis. To reduce the beam hardening effect, a high-energy X-ray beam was used in the present study, and aluminum was used to filter the soft waves before transmission.

Following similar methodology, 2D distributions of $C\overline{C}$ for SR and WR were calculated, and the obtained 2D $C\overline{C}$ renderings are presented in Fig. 6.

A very irregular carbonation front shape is exhibited in Fig. 6, which suggests that specimens after mass balancing were not intact, either. Nevertheless, carbonation speed was much slower in mass-balanced specimens, and in particular, the carbonation depth of SR was approximately 3 mm at 2 days of carbonation, which was the smallest among the four series of specimens at that carbonation age. Considering the existence of side carbonation in mass-balanced specimens, this work did not show reduced carbonation rate due to the preserved microstructure; instead, higher moisture content near specimen surface was taken as the main explanation. As less gaseous space existed near the surface of mass-balanced samples, CO_2 transmission was hindered, which lead to reduced carbonation rates.

Correspondingly, 1D $C\overline{C}$ profiles for SR and WR are presented in Fig. 7. Similar to Fig. 5, a fast progressing carbonation front is exhibited. Compared with oven-dried specimens, the moisture movement was more restricted in these two tests, which can be

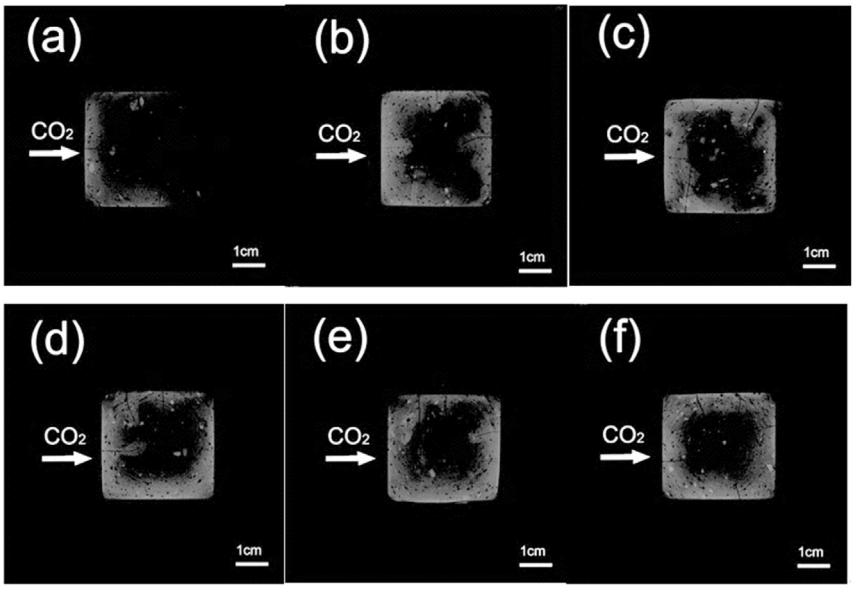

Fig. 6. 2D $C\overline{C}$ renderings at variant carbonation ages. (a), (b), (c) refer to SR after 2days, 7 days and 14 days of carbonation, respectively, and (d), (e), (f) refer to WR after 2 days, 7 days and 14 days of carbonation, respectively.

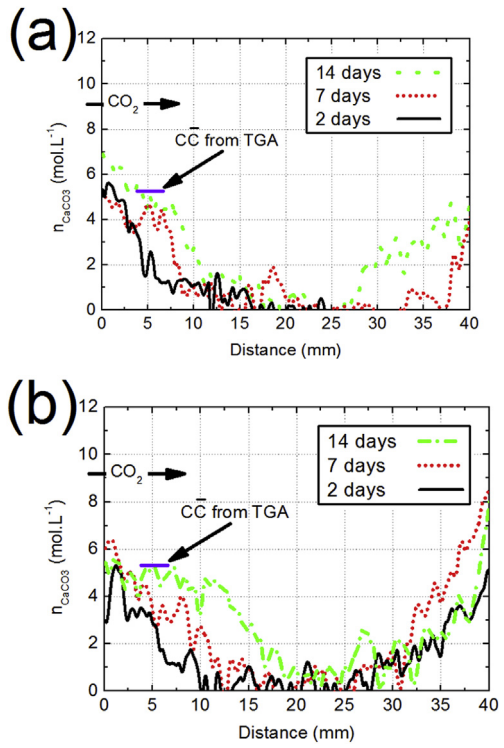

Fig. 7. 1D $C\overline{C}$ profiles for (a) SR and (b) WR. The purple bar represents the $C\overline{C}$ content measured through TGA. (For interpretation of the references to color in this figure legend, the reader is referred to the Web version of this article.)

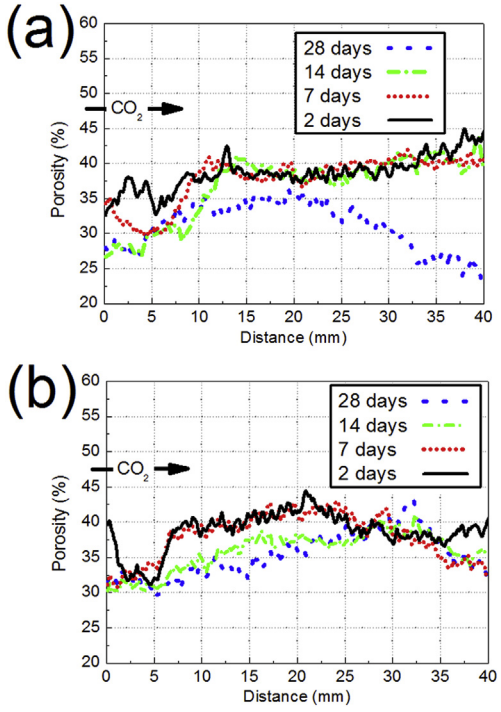

Fig. 8. 1D Porosity profiles for (a) SO and (b) WO. Carbonation progress could be revealed from the advancing front-ends on the profiles.

reflected from two aspects: first, unlike the $C\overline{C}$ profiles in Fig. 5, in Fig. 7, the $C\overline{C}$ content near the surface is similar with that inside at 2 days of carbonation, which proves the absence of excessive dryness; and, second, the $C\overline{C}$ content obtained from XRAM agrees well with that obtained from TGA, which reveals that the moisture movement could be ignored for the mass-balanced specimens.

3.3. Microstructure evolution obtained through XRAM and MIP

Based on the chemical results, the carbonation mechanism and the extent of carbonation were similar among the four series of specimens (see Figs. 5 and 7), which further implies that the variation of carbonation behavior was mainly as a result of other factors, like variations in microstructure or variations in moisture distribution. By using XRAM, it is now possible to investigate both these factors.

1D distributions of local porosity were deduced through Eq. (3)

and are shown in Fig. 8. Similar to Figs. 5 and 7, the 1D profiles are the average result of 5000 instant profiles. For both SO and WO, the local porosity was reduced by ~30% by carbonation. Nearly unanimous consensus has been reached toward the porosity reduction by carbonation in cement-based materials [41]: since the molar volume of carbonation product is larger than that of the reactant, the fine carbonation product can fill the pores, leading to porosity reduction. Besides, based on the similar magnitude of reduced porosity, the work further confirms that the extent of carbonation was similar between SO and WO.

In line with 1D $C\overline{C}$ profiles, the carbonation depth can be read from the 1D porosity profiles. Compared with results from phenolphthalein indicator or from $C\overline{C}$ profiles, these results show a good agreement among each other, which confirms that all three parameters are suitable for carbonation detection. According to 2-day profiles in Fig. 8(a) and (b), the excessive dryness can be seen again, as the porosity was less reduced near the surface. The excessive dryness was no longer observable at 7 days of carbonation, which also agrees well with the chemical results.

1D porosity profiles for SR and WR are presented in Fig. 9. Similar to Fig. 8, a reduced porosity by carbonation is revealed. The progress of carbonation can still be seen from the porosity profile; however, due to broader carbonation front, the carbonation depth cannot be measured precisely (see Fig. 9). A broader carbonation front in mass-balanced specimens was the result of a greater surface damage. CO_2 would be preferentially transported through the cracks, the overall reaction was no longer controlled by diffusion, and an irregular-shaped carbonation front would occur.

Even though XRAM is versatile, the method is only capable of offering the information of porosity, while information on pore distribution is unavailable through it. However, to figure out microstructure evolution during carbonation, the information of pore size distribution (PSD) is essential. The PSD curves in this study were obtained from mercury intrusion porosimetry (MIP) test, and the results are illustrated in Fig. 10. To be representative,

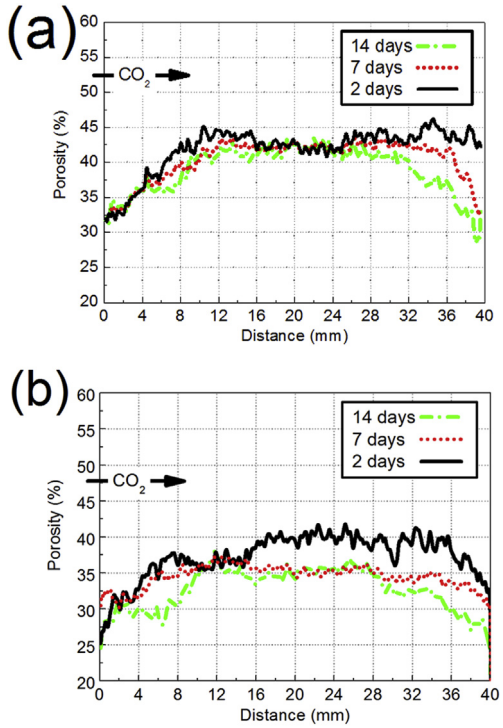

Fig. 9. 1D porosity profiles for (a) SR and (b) WR.

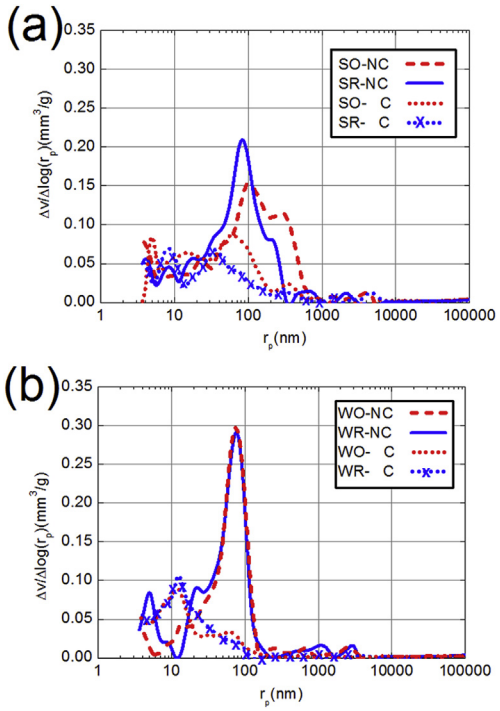

Fig. 10. Pore size distribution curves for (a) Standard-cured specimen and (b) Water-cured specimen.

each curve in Fig. 10 is the average result of two independent PSD curves.

As shown in Fig. 10, the threshold pore radius is approximately 100 μm for all tests before the start of carbonation and only the peak interval is broader for standard-cured specimens. The population of large pores ($r > 100$ nm) is bigger for standard-cured specimens, which is most probably due to the better-developed microstructure in water-cured specimens. When SR and SO specimens are compared, the peak interval of SR is narrower, which confirms that hydration could continue during mass-balancing process.

After carbonation, the population of pores for all specimens are invariably reduced, which is consistent with the result from XRAM. Again, complying with previous researchers, pore clogging effect was seen as the main reason for porosity reduction.

3.4. Investigation of moisture migration by XRAM

It is difficult to carry out investigation on moisture evolution through traditional techniques, as these processes would inevitably alter the moisture distribution inside the samples. By using XRAM, the local moisture content can be addressed quantitatively.

1D moisture profiles for SO and WO are shown in Fig. 11. Right after preconditioning, the water content was lower at both ends of the moisture profiles, which is reasonable considering the excessive dryness. The moisture content at the carbonation end was recovered after 7 days of carbonation, which can be explained in two ways: first, the RH level was higher inside the carbonation chamber, and the moisture inside the chamber could serve as the reservoir; and, second, carbonation reaction produced water, and the released water could increase the moisture content near the carbonation end.

Accordingly, the moisture distributions for SR and WR were calculated and are shown in Fig. 12. Compared with Fig. 11, the water content near both ends was relatively higher, and the

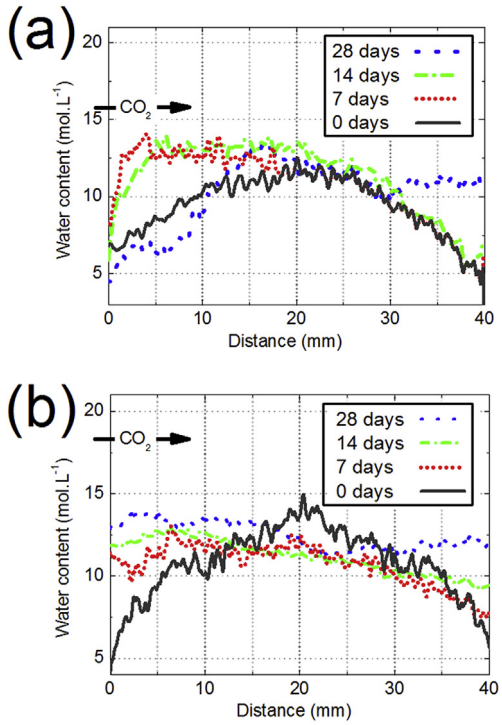

Fig. 11. 1D moisture profiles for (a) SO and (b) WO. The water content is lower near both ends of profiles at 0 day, revealing the excessive dryness. The water content near the carbonation face kept increasing throughout carbonation for WO, while for SO, the increasing trend stopped at 14 days, and the moisture content decreased afterwards.

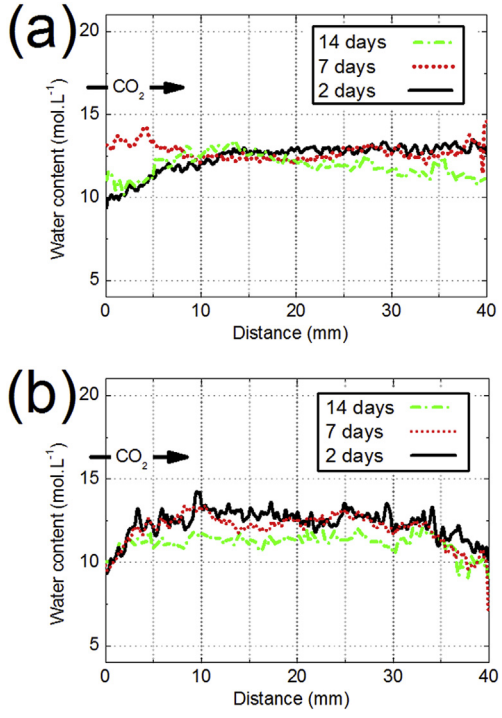

Fig. 12. 1D moisture profiles for (a) SR and (b) WR, respectively. The moisture distribution is more uniform compared with Fig. 11, which confirms that mass balancing is effective.

moisture gradient was smaller at 0 day. This confirms that mass balancing is a suitable drying protocol, as it produces specimens with a uniform moisture distribution.

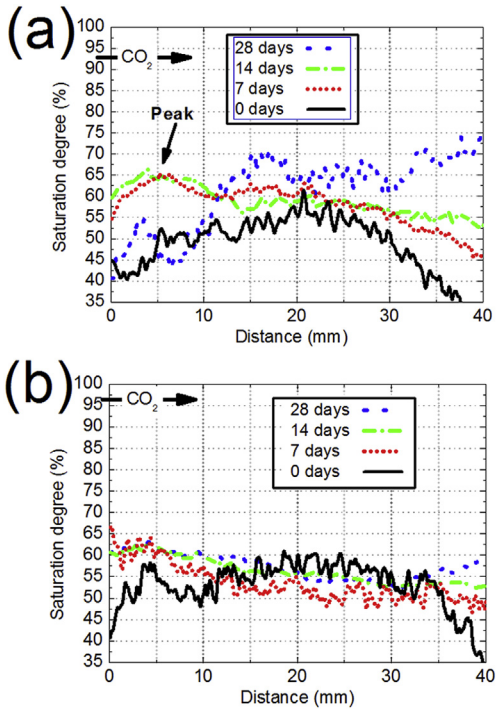

Fig. 13. 1D distribution of local saturation degree for (a) SO and (b) WO.

3.5. Evolution of saturation degree (SD) during carbonation

In this study, both local water content and local porosity were obtained; combining both parameters, the local saturation degree (SD) could also be calculated, as expressed by Eq. (4).

$$S = \frac{W}{P} \times 100\% \tag{4}$$

where, S, W and P are the local saturation degree, the local water content and the local porosity, respectively.

1D SD profiles for SO and WO are presented in Fig. 13. The curves evolved in a similar pattern with those in Fig. 11, which suggests that the evolution of saturation degree was mainly controlled by the alteration of moisture content and not by the alteration of porosity. The excessive dryness is still observable, as both ends of the SD profiles are of lower SD compared with that near the core area. The local SD near the carbonation end recovered gradually during carbonation, which is consistent with the moisture profiles in Fig. 11. A peak was revealed on the SD profiles for SO at 7 and 14 days of carbonation, considering the peak was not observable on the related moisture profiles, pore refinement was referred here to explain its existence. The SD near carbonation end fell back at 28 days of carbonation for SO; however, for WO, the increasing trend maintained throughout the carbonation process, which suggests that microstructure in SO was more connected and moisture transmission was easier under that circumstance.

1D SD profiles for SR and WR are presented in Fig. 14. As expected, a more uniform saturation was achieved by mass balancing, which highlights the effectiveness of mass balancing in controlling inner RH. In both SR and WR cases, a peak, representing a perturbance of saturation degree, is observable at two days, and similar with oven-dried specimens, porosity reduction, together with an increased moisture content, were resorted to as the explanation. The peak vanished at 7 days of carbonation, which revealed the existence of a moisture re-equilibrium process.

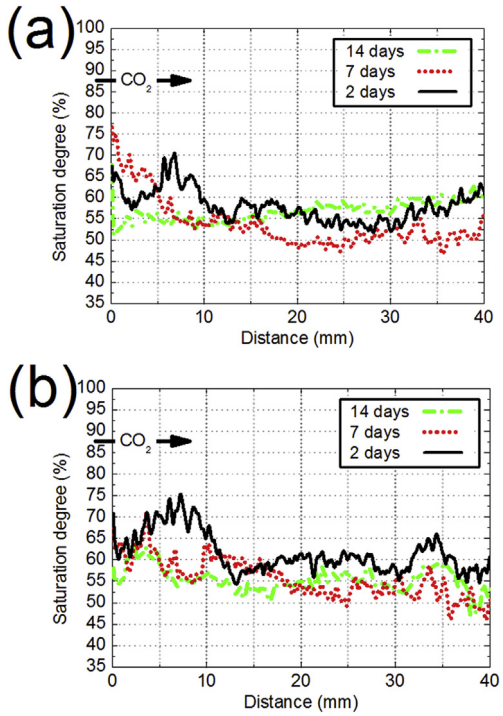

Fig. 14. 1D distribution of local saturation degree for (a) SR and (b) WR.

4. Discussion

4.1. Porosity variation through MIP and through XRAM

In the present study, both MIP and XRAM are adopted for porosity calculation. Compared with porosity measured through XRAM, the porosity measured through MIP was smaller, which is reasonable. In MIP, mercury is used as the intrusion medium, and the material can only intrude capillary pores and some gel pores (with pore radii larger than 3 nm in the present study); however, in XRAM, since water is used as the intrusion medium, the method can easily access a wider range of pores [16,17,33].

The porosity was nearly the same among four test series regardless of the use of MIP or XRAM (see Fig. 15). The result implies that, porosity may not be an effective parameter in characterizing the damage caused exclusively by preconditioning. A better method needs to be developed for damage characterization.

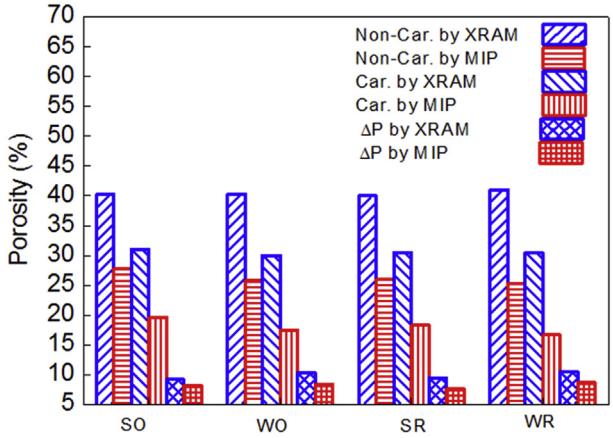

Fig. 15. Porosity and porosity variation by carbonation measured through XRAM or through MIP.

The variation of porosity during carbonation is at a similar order of magnitude based on XRAM and MIP, as shown in Fig. 15 which confirms that, fine pores (with a radius smaller than 3 nm and thus can only be accessed by XRAM) remained unchanged during carbonation.

4.2. Evaluation of damage extent through side carbonation

As shown in Fig. 15, no clear difference of porosity was revealed among four series, which implies that neither MIP nor XRAM was capable of characterizing the damage extent by preconditioning. Besides, due to limitation of CT's resolution, the damage cannot be evaluated directly by CT scanning [42,43]. Nevertheless, based on the side carbonated areas in the 2D $C\overline{C}$ renderings (see Figs. 4 and 6), all specimens were damaged after preconditioning. Therefore, it is essential to evaluate the damage for each preconditioning scheme.

In order to figure out the optimal preconditioning scheme for carbonation, the damage incurred by preconditioning should be taken for investigation. To fulfill that, an indirect method is introduced here. As shown in Fig. 16, a series of reconstructed images were presented. The images were collected from the 2D cross-sectional area 0.5 mm, 1.0 mm, 1.5 mm, 2.0 mm and 2.5 mm respectively beneath one lateral face, and the lateral face was adjacent to the carbonation face, thus sealed with epoxy resin throughout the carbonation tests.

According to Fig. 16, even though the lateral face was sealed by epoxy resin, side carbonation could not be prevented, and its extent was even higher on the slices closer to the surface. This highlights the deficiency of epoxy resin in controlling the side carbonation: even though the lateral surface was sealed, the cracks went to a deeper area, thus could not be completely blocked by resin on specimen surface. When CO_2 transported through the specimens, it preferentially diffused through the cracks. Even though the cracks may be beyond the resolution of a CT scanner, their paths could be "highlighted" by the carbonation of crack paths (see the bright strips in Fig. 16). Therefore, through tracing side carbonated area, the degree of surface damage can be evaluated.

To validate the connection between side carbonation and surface damage, the same specimen was dried at 45 °C for two more weeks, and an additional CT scan was performed. This second CT image obtained from the location identical to Fig. 16(f) was rendered and is shown in Fig. 16(f). Drying is expected to cause crack propagation, which makes crack observations easier. The crack morphology in Fig. 16(f) shows good consistency with the bright strips in Fig. 16(a)-(e), which reconfirms the connection between surface damage and side carbonation.

Based on above discussion, Figs. 4 and 6 were revisited for the evaluation of extent of damage due to drying. According to Fig. 4, the extent of damage extent near the surface was higher for water-cured specimen, as in this case the side carbonation occupied a wider area, and its casting face was already fully carbonated after 2 days of carbonation (see Fig. 4(d)). For SR and WR, side carbonation was observable from both specimens, which confirms that mass balancing would also bring additional, unspecified damage to the specimen. Unlike SR, the side carbonated area was already quite significant at 2 days of carbonation for WR, which attests again, the damage extent of water cured specimens is higher. Two possible reasons can be given here for the higher damage extent in water-cured campaigns: first, the initial RH was higher in water-cured samples right after curing, so the RH gap between the sample and the environment was larger. The larger RH gap incurred higher capillary forces, leading to greater extent of damage; and, second, moisture migration seemed to be more difficult for water-cured specimen, as larger SD gradient was observed after drying in WO

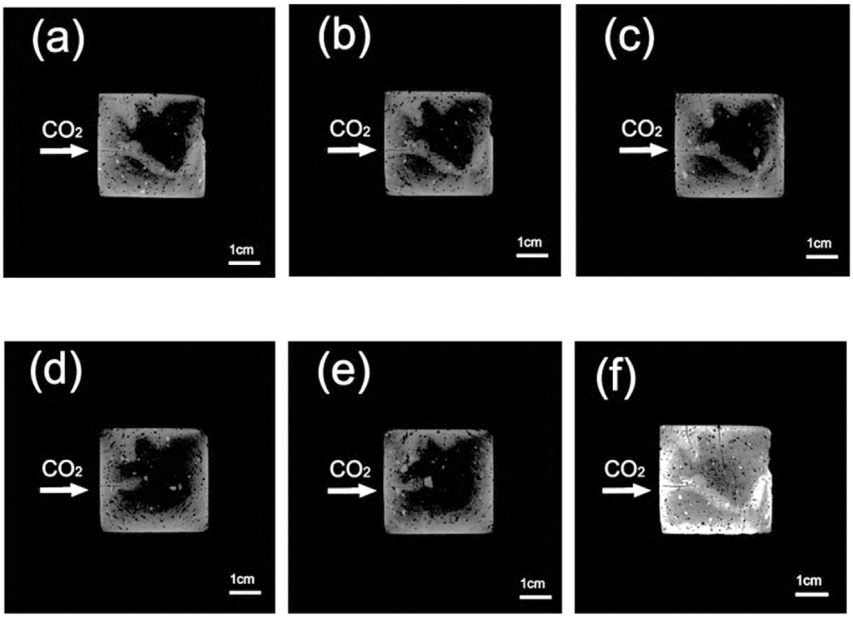

Fig. 16. 2D $C\bar{C}$ distributions rendered from (a) 0.5 mm, (b) 1.0 mm, (c) 1.5 mm, (d) 2.0 mm and (e) 2.5 mm beneath the surface of one side face. (f) refers to the CT slice obtained from the location identical with (a) after drying.

(see Fig. 13). The larger SD gradient in the specimens could also incur larger shrinkage force, leading to higher extent of damage.

4.3. Evolution of local RH

Spatial distribution of RH cannot be obtained directly from XRAM. Luckily, for the paste used in this study (with a water to cement ratio of 0.5), its water vapor desorption isotherms have been already built by previous researchers (see Fig. 17) [44]. Hence, following the desorption isotherm curves, the SD profiles in Fig. 13 and in Fig. 14 can be translated into the RH profiles, and an investigation of the RH evolution, was thereby possible. It should be noted that due to the existence of ink-bottle pores, a desorption isotherm curve is not overlapped with an absorption isotherm curve (a hysteresis effect). For the specimens directly after preconditioning, the translated RH should be quite precise, as the samples had just suffered from a moisture loss; however, for samples at later age, the evaluated RH should be on some extent overestimated, as the samples might go through some absorption process and no longer obey the desorption isotherm curves. Nonetheless, the RH profiles obtained here was applied for qualitative evaluation of the evolving pattern of local RH; therefore, even though the RH value may not be precise, the uncovered trend for RH evolution should still be of significance.

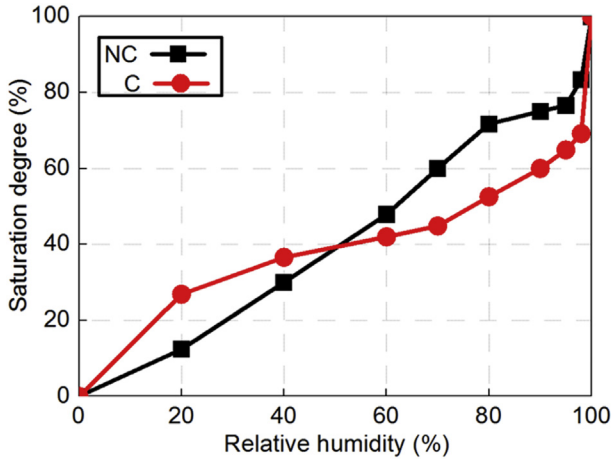

Fig. 17. Water vapor desorption isotherms of paste made with Portland cement before and after carbonation (W/C of 0.5 [44]).

1D distributions of RH are shown in Fig. 18. The RH profiles before carbonation are displayed as continuous curves, while the profiles after carbonation are presented in an intermitted way, which is based on two considerations: first, carbonation front is of an irregular shape, it is therefore, difficult to define the carbonation status near that boundary area, and RH translation is then incapable around that area; and, second, sample surface suffered from unspecified damage during carbonation, which altered the microstructure, and the desorption behavior near the sample surface may not comply with the desorption isotherm curves in Fig. 17.

Consistent with moisture profiles and SD profiles, the local RH near specimen surface was lower after thermal pretreatment; besides, similar with SD profiles, a narrower gradient interval with a larger SD gradient, is revealed for WO, which confirms that moisture migration was more difficult for water-cured specimens. The local RH increased for all cases after carbonation, aside from an increased local water content, the refined microstructure, could also be cited as one explanation.

Compared with WO, the RH increase was less pronounced for SO specimens at 28 days, which is reasonable given that moisture migration was easier in standard-cured specimens. For mass-balanced specimens, the RH profiles fluctuated less, which confirms a mild moisture migration throughout duration of the carbonation test.

Based on the RH profiles, it seems to be impractical to hold the RH at a constant level during carbonation, as both water-releasing effect and pore-refining effect will increase the local RH. Nonetheless, mass-balancing is still a better choice, as the RH fluctuation would be restricted to a smaller extent during carbonation.

It should be mentioned that in previous studies, parabolic curves were commonly used to present the relationship between

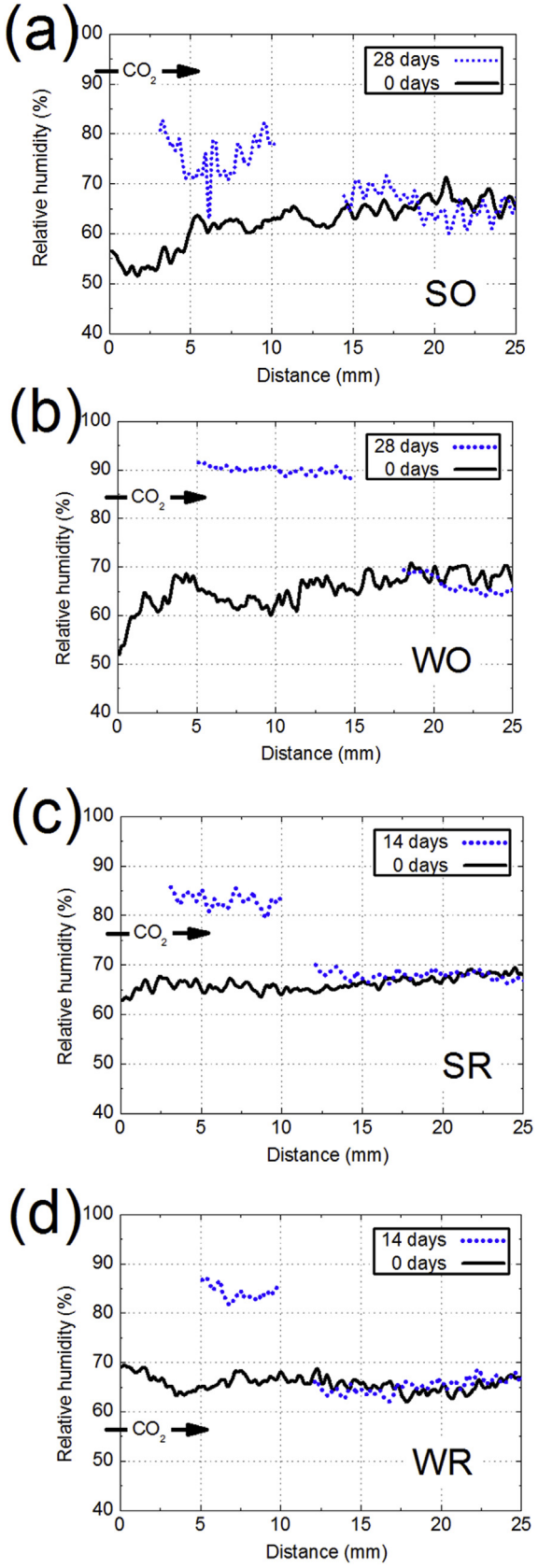

Fig. 18. 1D distribution of local RH for (a) SO; (b) WO; (c) SR, and (d) WR.

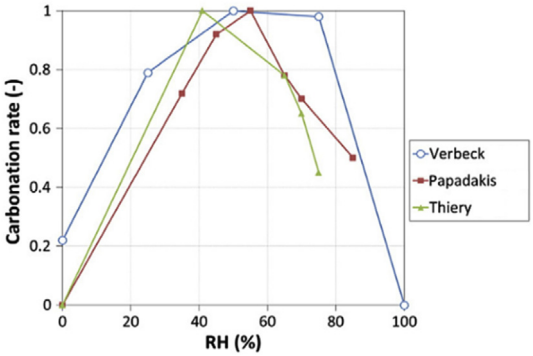

Fig. 19. Example of relationship between carbonation rate and RH [18].

the RH and the carbonation speed (see Fig. 19), and the curves were built either through experimental data [45] or through numerical modelling [18,41,46]. Based on the RH profiles in this study, the local area where carbonation occurred exhibited RH higher than that in the carbonation chamber. This means that, the real RH under which carbonation took place was underestimated. Judging from that parabolic curves built through experimental data should have an inflection point smaller than that built through numerical modelling.

5. Conclusions

In this research, carbonation of cement paste was studied. Four different pretreating protocols based on chemical changes, microstructure evolution and moisture migration during carbonation were selected and investigated. The following conclusions can be drawn from this study.

1) None of the preconditioning scheme is capable of fully preserving the microstructure. Compared with water-cured specimen, less damage would be incurred during preconditioning for standard-cured specimen.
2) Mass balancing is proved to be a more suitable drying protocol than oven drying, as excessive dryness can be prevented, and local moisture content is more uniform after balancing.
3) Based on the fact that similar contents of carbonation product were generated in all tests, it can be concluded that preconditioning schemes have an insignificant effect on the extent of carbonation. Even though the carbonation product from XRAM may not be precisely measured due to omission of moisture migration, the chemical results from XRAM were still comparable with those from TGA and thus were, reliable.
4) For all tests, local porosity was uniformly reduced by around 30% due to carbonation, which shows that similar carbonation mechanism and amount of carbonation occurred in all tests.
5) For oven-dried specimens, their moisture content was lower near the specimen surface, which led to an exaggerated carbonation depth at early ages. The moisture content near the carbonation surface, however, could be recovered in the first week itself. For mass-balanced specimens, their moisture content was more uniformly distributed, and less fluctuations were observed during carbonation.
6) The degree of saturation at various locations was seen to match the local moisture contents. Nonetheless, the peak noted exclusively on the SD profiles implies that microstructure evolution affects the local degree of saturation.
7) Water-cured specimens suffered a greater degree of damage due to side carbonation.

8) Through the use of desorption isotherm curves, the distribution of local relative humidity (RH) was obtained in this study. The RH profiles attest that local RH cannot be fixed during carbonation, as both the released water and the refined microstructure will disturb local RH. Nonetheless, using mass-balanced specimens, the RH would fluctuate to a smaller extent during carbonation.

Acknowledgements

Thanks are owed to the Natural Sciences and Engineering Research Council of Canada and Canada India Research Center of Excellence (IC-IMPACTS) for financial assistance. The work was performed at the University of British Columbia during the senior author's joint education period, funded by the Chinese Scholarship Council. Thanks are also given to Dr. Sudip Talukdar for his valuable help on paper writing.

References

[1] S. Talukdar, N. Banthia, Carbonation in concrete infrastructure in the context of global climate change: model refinement and representative concentration pathway scenario evaluation, J. Mater. Civ. Eng. 28 (4) (2015), 04015178.
[2] S. Talukdar, N. Banthia, Carbonation in concrete infrastructure in the context of global climate change: development of a service lifespan model, Constr. Build Mater 40 (Supplement C) (2013) 775–782.
[3] S. Talukdar, N. Banthia, J.R. Grace, Carbonation in concrete infrastructure in the context of global climate change: Part 2 – canadian urban simulations, Cem. Concr. Comp. 34 (8) (2012) 931–935.
[4] S. Talukdar, N. Banthia, J.R. Grace, Carbonation in concrete infrastructure in the context of global climate change – Part 1: experimental results and model development, Cem. Concr. Comp. 34 (8) (2012) 924–930.
[5] C.W. Hargis, Carbonation of calcium sulfoaluminate mortars, Cem. Concr. Comp. 80 (Supplement C) (2017) 123–134.
[6] S. Ruan, C. Unluer, Influence of mix design on the carbonation, mechanical properties and microstructure of reactive MgO cement-based concrete, Cem. Concr. Comp. 80 (Supplement C) (2017) 104–114.
[7] H. Chang, Chloride binding capacity of pastes influenced by carbonation under three conditions, Cem. Concr. Comp. 84 (Supplement C) (2017) 1–9.
[8] A. Leemann, F. Moro, Carbonation of concrete: the role of CO2 concentration, relative humidity and CO2 buffer capacity, Mater. Struct. 50 (1) (2017) 30.
[9] S. Hussain, D. Bhunia, S. Singh, Comparative study of accelerated carbonation of plain cement and fly-ash concrete, J. Biol. Eng. 10 (2017) 26–31.
[10] P. Mikhailenko, Influence of physico-chemical characteristics on the carbonation of cement paste at high replacement rates of metakaolin, Constr. Build. Mater. 158 (2018) 164–172.
[11] Y. Wang, Influence of combined carbonation and chloride ingress egimes on rate of ingress and redistribution of chlorides in concretes, Constr. Build. Mater. 140 (2017) 173–183.
[12] A.G. Magalhães, The influence of the water/cement ratio in the open porosity and in the carbonation front advancing in cementitious matrix composites, Appl. Mech. Mater. 864 (2017) 313–317.
[13] Y.C. Wang, P.A.M. Basheer, Progress of carbonation in chloride contaminated concretes, in: International Conference on Durability of Concrete Structures, 2016. Shenzhen, China, June 30-July 1.
[14] H. Samouh, E. Rozière, A. Loukili, The differential drying shrinkage effect on the concrete surface damage: experimental and numerical study, Cem. Concr. Res. 102 (2017) 212–224.
[15] C.S. Pillai, Evaluation of microstructural and microchemical aspects of high density concrete exposed to sustained elevated temperature, Constr. Build. Mater. 126 (2016) 453–465.
[16] A. Morandeau, M. Thiéry, P. Dangla, Impact of accelerated carbonation on OPC cement paste blended with fly ash, Cem. Concr. Res. 67 (Supplement C) (2015) 226–236.
[17] A. Morandeau, M. Thiéry, P. Dangla, Investigation of the carbonation mechanism of CH and C-S-H in terms of kinetics, microstructure changes and moisture properties, Cem. Concr. Res. 56 (Supplement C) (2014) 153–170.
[18] P. Turcry, Analysis of an accelerated carbonation test with severe preconditioning, Cem. Concr. Res. 57 (2014) 70–78.
[19] Z. Zhao, Improving properties of recycled concrete aggregates by accelerated carbonation, in: International Conference on Sustainability Construction Materials and Technologies, 2016.
[20] C. Bilim, C.D. Atiş, Carbonation resistance of slag mortars activated by different alkali activators, Tukish J. Eng. (TUJE) 1 (1) (2017) 1–4.
[21] A. Nassif, E. Burley, S. Ridgen, A new quantitative method of assessing fire damage to concrete structures, Mag. Concr. Res. 47 (172) (1995) 271–278.
[22] K. Ng, Investigation of internal frost damage in cementitious materials with micromechanics analysis, SEM imaging and ultrasonic wave scattering techniques, Constr. Build. Mater. 50 (2014) 478–485.
[23] F. Ghasemzadeh, M. Pour-Ghaz, Effect of damage on moisture transport in concrete, J. Mater. Civ. Eng. 27 (9) (2014), 04014242.
[24] L. Biolzi, S. Cattaneo, G. Rosati, Evaluating residual properties of thermally damaged concrete, Cem. Concr. Comp. 30 (10) (2008) 907–916.
[25] J. Gao, Durability of concrete exposed to sulfate attack under flexural loading and drying–wetting cycles, Construct. Build. Mater. 39 (2013) 33–38.
[26] C.S. Poon, Strength and durability recovery of fire-damaged concrete after post-fire-curing, Cem. Concr Res. 31 (9) (2001) 1307–1318.
[27] D.J. Janssen, Moisture in Portland cement and cement concrete, Transport. Res. Rec. (1121) (1987).
[28] L. Parrott, Moisture conditioning and transport properties of concrete test specimens, Mater. Struc. 27 (8) (1994) 460–468.
[29] K. Wan, 3D spatial distribution of the calcium carbonate caused by carbonation of cement paste, Cem. Concr. Comp. 45 (1) (2014) 255–263.
[30] K. Wan, 3D porosity distribution of partly calcium leached cement paste, Constr. Build. Mater. 48 (19) (2013) 11–15.
[31] G.B. T50082-2009, Standard for Test Methods of Long-term Performance and Durability of Ordinary Concrete, China Architecture and Building Press, Beijing, China, 2009, pp. 61–63.
[32] H.L. Ramandi, Porosity and permeability characterization of coal: a micro-computed tomography study, Int. J. Coal Geol. 154–155 (Supplement C) (2016) 57–68.
[33] D. Cui, Porosity characterization in interfacial transition zone using dual CT scans, J. Test. Eval. 45 (2) (2016) 408–418.
[34] E.M. Withjack, Computed tomography for rock-property determination and fluid-flow visualization, Spe. Form. Eval. 3 (3) (1988) 696–704.
[35] S. Latham, T. Varslot, A. Sheppard, Image Registration: Enhancing and Calibrating X-ray Micro-CT Imaging, Imaging Society of Core Analysts Paper No, 2008.
[36] N.I. Fattuhi, Concrete carbonation as influenced by curing regime, Cem. Concr. Res. 18 (3) (1988) 426–430.
[37] J.W. Carey, Analysis and performance of oil well cement with 30 years of CO2 exposure from the SACROC Unit, West Texas, USA. Int. J. Greenh. Gas. Con. 1 (1) (2007) 75–85.
[38] P.H.R. Borges, Carbonation of CH and C–S–H in composite cement pastes containing high amounts of BFS, Cem. Concr. Res. 40 (2) (2010) 284–292.
[39] M. Castellote, Chemical changes and phase analysis of OPC pastes carbonated at different CO2 concentrations, Mater. Struc. 42 (4) (2009) 515–525.
[40] R.A. Brooks, G. Chiro Di, Beam hardening in x-ray reconstructive tomography, Phys. Med. Biol. 21 (3) (1976) 390.
[41] V.G. Papadakis, C.G. Vayenas, M.N. Fardis, Fundamental modeling and experimental investigation of concrete carbonation, Aci. Mater. J. 88 (4) (1991) 363–373.
[42] A.C. Bordelon, J.R. Roesler, Spatial distribution of synthetic fibers in concrete with X-ray computed tomography, Cem. Concr. Comp. 53 (2014) 35–43.
[43] J. Moon, Characterization of a sustainable sulfur polymer concrete using activated fillers, Cem. Concr. Comp. 67 (2016) 20–29.
[44] M. Auroy, Impact of carbonation on unsaturated water transport properties of cement-based materials, Cem. Concr. Res. 74 (2015) 44–58.
[45] H.J. Wierig, Longtime studies on the carbonation of concrete under normal outdoor exposure, in: Proceedings RILEM Seminar on the Durability of Concrete Structures under Normal Outdoor Exposure, 1984, pp. 239–249.
[46] B. Salvoldi, Oxygen permeability of concrete and its relation to carbonation, Constr. Build. Mater. 85 (2015) 30–37.